nature materials

ARTICLES

https://doi.org/10.1038/s41563-021-01161-6

Inter-facet junction effects on particulate photoelectrodes

Xianwen Mao[1,2] and Peng Chen[1]✉

Particulate semiconductor photocatalysts are paramount for many solar energy conversion technologies. In anisotropically shaped photocatalyst particles, the different constituent facets may form inter-facet junctions at their adjoining edges, analogous to lateral two-dimensional (2D) heterojunctions or pseudo-2D junctions made of few-layer 2D materials. Using subfacet-level multimodal functional imaging, we uncover inter-facet junction effects on anisotropically shaped bismuth vanadate ($BiVO_4$) particles and identify the characteristics of near-edge transition zones on the particle surface, which underpin the whole-particle photoelectrochemistry. We further show that chemical doping modulates the widths of such near-edge surface transition zones, consequently altering particles' performance. Decoupled facet-size scaling laws further translate inter-facet junction effects into quantitative particle-size engineering principles, revealing surprising multiphasic size dependences of whole-particle photoelectrode performance. The imaging tools, the analytical framework and the inter-facet junction concept pave new avenues towards understanding, predicting and engineering (opto)electronic and photoelectrochemical properties of faceted semiconducting materials, with broad implications in energy science and semiconductor technology.

Particulate semiconductor photocatalysts are promising systems for solar-to-fuel technologies[1–12]. In such catalytic systems, one critical factor for attaining high energy conversion efficiencies is the effective separation of photogenerated electrons and holes within individual particles to prevent charge-carrier recombination[1–11]. Recent studies show that charge-carrier separation can be facilitated using anisotropically shaped semiconductor particles exposing facets with different work functions[1,2,6]. This difference in work function leads to preferential charge-carrier accumulation on different facets, suppressing surface electron–hole recombination, although this difference is generally not large enough to generate a surface current across the different facets (that is, surface confined charge separation)[13,14]. While previous studies of anisotropically shaped semiconductor particles recognize the differences in work function and the associated charge-carrier activities among different facets, they all assume no variations of these properties within the same facet[1,2,6].

Here we hypothesize that within each anisotropically shaped photocatalyst particle, the different constituent facets may form inter-facet junctions at their adjoining edges (Fig. 1a) analogous to lateral two-dimensional (2D) heterojunctions or pseudo-2D junctions made of few-layer 2D materials[15–19], and that these inter-facet junctions should lead to spatial variations of electronic and photoelectrochemical properties along the particle surface even within the same facet at near-edge regions. These inter-facet edges resemble one-dimensional (1D) interfaces of lateral 2D junctions (Fig. 1b); the valence and conduction band levels at the surface (E_V^{surf}, E_C^{surf}) would bend near these edges, forming near-edge transition zones along the facet surface (Fig. 1b, red lines). We further hypothesize that if the surface transition zone width becomes comparable to the overall particle size (which is likely considering that lateral 2D junctions are known to have broad depletion zones[20–22]), such surface band bending should substantially influence the overall (opto) electronic properties and performance of the whole particle towards applications such as (photo)electrocatalysis, important for renewable energy technologies[1,4,7–9,12,23,24]. Whether these hypotheses are true is completely unknown, however.

Moreover, such inter-facet junctions are notably not identical to ideal lateral 2D heterojunctions. The inter-facet junctions exhibit a higher degree of complexity—the junction-forming near-surface structures on each facet, which have distinct electronic properties from the particle interior, are not strictly confined to the top single layer of surface atoms and may comprise several subsurface atomic layers. Also the electric field generated by the work function difference between adjoining facets may vary both along the particle surface and towards the particle interior. Therefore, it is challenging to predict the effects of such inter-facet junctions and the associated intra-facet variations of functional properties, let alone under realistic operando conditions.

In this work, using subfacet-level multimodal functional imaging, we uncover inter-facet junction effects and associated intra-facet variations of photoelectrochemical properties in anisotropically shaped $BiVO_4$ particles under photocatalyst working conditions (that is, under illumination and electrochemical control, in an aqueous electrolyte, and with water oxidation occurring). We identify the key characteristics of the inter-facet junctions that dictate whole-particle photoelectrochemistry, including the near-edge surface transitions of local flat-band potential and charge separation efficiency at the solid-electrolyte interface (SEI). We further show that chemical doping modulates the widths of the surface transition zones near the inter-facet edge, consequently altering the overall performance of photocatalyst particles. Decoupled facet-size scaling laws further translate inter-facet junction effects into quantitative particle-size engineering principles, revealing surprising multiphasic size dependences of whole-particle photoelectrode performance. The imaging tools, analytical framework and inter-facet junction concept pave new avenues towards understanding, predicting and engineering (opto)electronic and photoelectrochemical properties of faceted semiconducting materials, with broad implications in

[1]Department of Chemistry and Chemical Biology, Cornell University, Ithaca, NY, USA. [2]Present address: Department of Materials Science and Engineering, National University of Singapore, Singapore, Singapore. ✉e-mail: pc252@cornell.edu

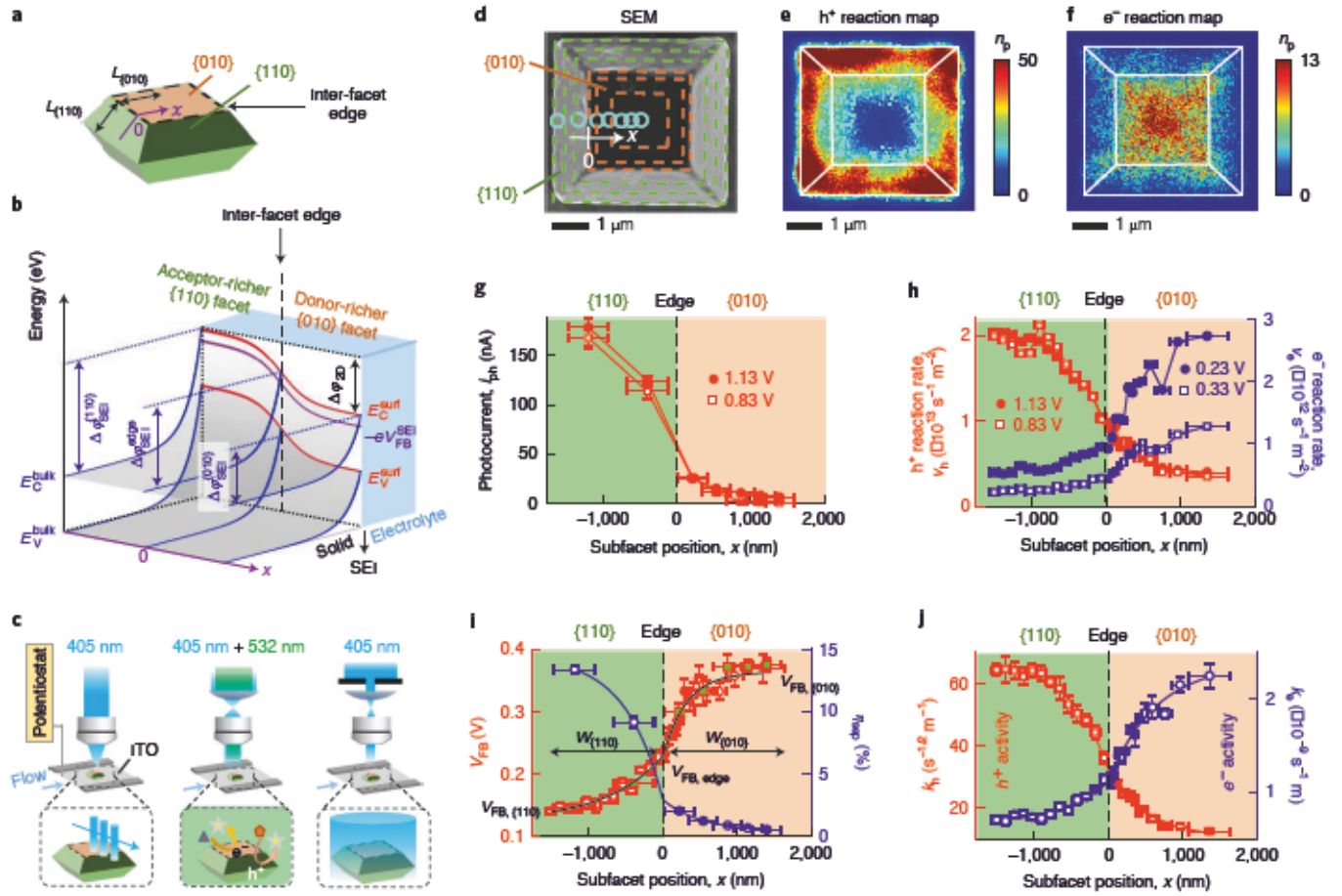

Fig. 1 | Visualizing inter-facet junction effects in anisotropically shaped semiconductor particles. a, Schematic illustration of an anisotropically shaped $BiVO_4$ particle with exposed {010} and {110} facets. $L_{\{010\}}$ ($L_{\{110\}}$) quantifies the {010} ({110}) facet size. The *x* axis is defined to be along the facet surface ($x = 0$, inter-facet edge; $x > 0$, {010} facet; $x < 0$, {110} facet). **b**, Envisioned energy diagram demonstrating inter-facet junction effects in an anisotropically shaped $BiVO_4$ particle in contact with an electrolyte. SEI, solid–electrolyte interface. **c**, Multimodal functional imaging set-up (Methods) comprising a microfluidic photoelectrochemical cell with individual particles dispersed on an ITO electrode, under three different laser illumination configurations. Left, focused 405 nm laser excitation for subfacet-level photoelectrochemical current mapping. Middle, wide-field epifluorescence illumination for super-resolution charge-carrier reaction imaging; 532 nm laser excites the reaction product fluorescence. Right, iris-confined illumination for single-whole particle photoelectrochemical current measurement. **d**, SEM image of a representative $BiVO_4$ particle examined in **e**–**j**. Dashed lines, facet dissections. Circles, size and position of focused 405 nm laser. **e**,**f**, Super-resolution images of h+ (potential ≥ 0.93 V) (**e**) and e− (potential ≤ 0.63 V) (**f**) induced reactions. n_p, number of detected product molecules. Bin size, 37.1 nm². White lines, structural contours from SEM in **d**. Imaging duration (each potential), 22.5 min. **g**,**h**, Subfacet-position dependences of i_{ph} (**g**), v_h and v_e (**h**) at selected potentials. For data at all potentials see Supplementary Fig. 13. Solid lines connect points. **i**,**j**, Subfacet-position dependences of V_{FB} (green-filled red squares, determined from i_{ph} in **g**; white-filled red circles, determined from v_h and v_e in **h**), η_{sep} (**i**), k_h and k_e (**j**). Solid lines, fits with equation (1). *y* error bars, s.d.; *x* error bars, measurement resolution or size of dissected region (Supplementary Fig. 3).

fields ranging from photo(electro)catalysis and energy science to electronics, photonics and related semiconductor technologies.

Visualizing inter-facet junction effects

We chose to study $BiVO_4$ because of its promise as a high-performance photoanode material for water oxidation (bandgap ~2.4 eV; valence band edge ~2.4 V versus reversible hydrogen electrode (RHE))[1,4–6]. We synthesized anisotropically shaped $BiVO_4$ particles with a truncated bipyramidal morphology, exposing {010} and {110} facets with tunable facet sizes ($L_{\{010\}}$, $L_{\{110\}}$: ~100 nm to tens of micrometres; Fig. 1a and Supplementary Fig. 8a). The {010} facet is lower in electron energy (that is, larger work function) and richer in oxide ion (O^{2-}) (which can act as an electron donor); the {110} facet is higher in electron energy (that is, smaller work function) and richer in bismuth (III) ion (Bi^{3+}) (which can act as an electron acceptor) (Supplementary Fig. 9)[6]. The {010}|{110} edge therefore constitutes a 1D interface, giving rise to an inter-facet junction, which should in turn lead to intra-facet variations of E_C^{surf} and E_V^{surf} along the particle surface (Fig. 1b, red lines). Importantly, on contacting electrolytes, this inter-facet junction should give rise to a location-dependent band bending degree ($\Delta\varphi_{SEI}$) across the SEI perpendicular to the facet: shallower bending on the donor-richer {010} facet, steeper bending on the acceptor-richer {110} facet and varying continuously across the inter-facet edge (Fig. 1b, blue lines). We envisioned that this $\Delta\varphi_{SEI}$ variation should lead to subfacet position (*x*)-dependent photoelectrochemical currents, a key photoelectrode performance metric.

We therefore focused a 405 nm laser to probe photoelectrochemical currents locally, and systematically scanned the focused laser spot along the *x* direction across the inter-facet edge on a single $BiVO_4$ particle (Fig. 1c, left; Methods). Correlated with scanning electron microscopy (SEM) (Fig. 1d), we measured, at a subfacet

resolution (~380 nm) (Supplementary Fig. 1b), the local steady-state anodic photoelectrochemical current (i_{ph}) associated with water oxidation at various potentials (all referenced to RHE)[10]. Strikingly, i_{ph} differs not only between different facets, but also within the same facet at near-edge regions, showing an *s*-like monotonic increase from the centre of the {010} facet ($x>0$), across the inter-facet edge ($x=0$) and into the {110} facet ($x<0$) (Fig. 1g). This spatial pattern, agreeing qualitatively with our hypotheses (Fig. 1b), suggests that inter-facet junction effects exist on anisotropically shaped semiconducting particles and influence particles' photoelectrochemistry. If there were no inter-facet junction effects, local photoelectrochemical currents within the same facet would have been invariant and would have exhibited a non-continuous, nearly abrupt change at the inter-facet edge. Moreover, the observed intra-facet spatial variation of photoelectrochemical current along the particle surface spans a micrometre-sized length scale, reminiscent of the characteristic broadness of depletion zones typically observed in lateral 2D junctions[20–22].

To probe local photoelectrochemical properties beyond the diffraction-limited resolution, we performed single-molecule super-resolution microscopy with redox-selective fluorogenic probes to map surface reactions induced by photogenerated holes (h^+) or electrons (e^-) at approximately 40 nm resolution while applying a range of potentials (Fig. 1c, middle; Methods)[10]. In this type of super-resolution microscopy, the single-molecule level wide-field imaging of the fluorescent reaction products enables individual localization of their positions down to nanometre precision as well as quantitative molecular counting under operando conditions[25–29]. At anodic potentials (for example, >0.5 V), h^+-induced reactions on this $BiVO_4$ particle occur less frequently on the donor-richer {010} facet than the acceptor-richer {110} facet (Fig. 1e), consistent with SEM studies of bulk-level photocatalytic deposition of solid-state oxidation or reduction catalysts onto $BiVO_4$ particles[6]. However, while this bulk-level study shows that holes (or electrons) preferentially accumulate on different facets, it does not probe intra-facet variations of charge-carrier activities. In contrast, here, using single-particle super-resolution reaction imaging, we reveal a spatial variation of surface hole activities even within the same facet (also for surface electron activities; below): the specific rate of h^+-induced reaction (v_h) shows a striking *s*-like, micrometre-sized spatial trend along the *x* direction (Fig. 1h, red), which parallels that of the local anodic photoelectrochemical current (dominated by h^+-induced water oxidation reaction; Fig. 1g) but possesses approximately ten times higher spatial resolution.

At less anodic potentials (for example, <0.6 V), e^--induced surface reactions are also detectable even though the overall photoelectrochemical current is anodic (Fig. 1f). Importantly, its specific rate v_e shows an *s*-like spatial trend along the *x* direction opposite to that of v_h (Fig. 1h, blue), again exhibiting an intra-facet variation. All subfacet-level quantities (v_h, v_e and i_{ph}) were corrected for intra-particle illumination attenuation (see Supplementary Note 1.8 in the Supplementary Information). Control experiments and analyses show that these spatial trends are not due to structural effects of low-coordination edge sites, preferential adsorption of probe molecules, or unequal fluorescence detection of reaction products (Supplementary Notes 2.3–2.5).

A modified Reichman model[10,30] allowed us to analyse and fit satisfactorily the potential dependences of local photoelectrochemical currents and h^+/e^--induced reaction rates (Supplementary Notes 1.3 and 1.7). In addition, we obtained intrinsic, potential-independent, parameters that govern photoelectrochemical water oxidation performance at the solid–electrolyte interface, including: the flat-band potential (V_{FB}), the electron–hole separation efficiency in the depletion zone at the SEI (η_{sep}) and the effective rate constant k_h (k_e) reflecting the surface hole (electron) activity. V_{FB} of this particle shows an *s*-like transition along the *x* direction across the {010}|{110} edge (Fig. 1i, red), as we hypothesized for the inter-facet transition zones on a particle's surface (Fig. 1b, purple line). More importantly, this transition along the particle surface spans over a micrometre length scale, which is substantially larger than the typical depletion zone width of bulk $BiVO_4$ junctions (<10 nm)[4]. Such broadness of the near-edge transition zones suggests that this inter-facet junction is analogous in electronic property to lateral 2D junctions, which exhibit broader depletion zone widths than do three-dimensional (3D) bulk junctions[20–22]. These observations provide a direct mapping of inter-facet junction effects within an anisotropically shaped semiconductor particle.

η_{sep} also exhibits an *s*-like transition along the *x* direction across the inter-facet edge over the same length scale (Fig. 1i, blue), but opposite to that of V_{FB}, expectedly, as steeper SEI band bending is associated with more efficient charge separation at SEI. k_h and k_e show anticorrelated, *s*-like inter-facet spatial trends over similar length scales (Fig. 1j). The k_h trend follows that of η_{sep} because surface hole activities of photoanodes contain SEI charge separation efficiency; the k_e versus k_h anticorrelation results from the electronic effect of the inter-facet junction (Supplementary Note 1.7). Moreover, the spatially resolved determination of V_{FB} and η_{sep} allows for predicting photoelectrochemical currents at any potential for any subfacet positions (see below).

Junction effects on whole-particle photoelectrochemistry

We examined many $BiVO_4$ particles; all of them exhibit subfacet position-dependent photoelectrochemical currents and charge-carrier surface activities, giving universal *s*-like inter-facet spatial variations of photoelectrochemical parameters (that is, V_{FB}, η_{sep}, k_h, k_e; Supplementary Fig. 15) across the particle surface. These *s*-like trends can be modelled satisfactorily as bidirectional exponential decays along the *x* direction from the edge (for example, Fig. 1i, solid line on V_{FB}), following the band bending modelling of lateral 2D junctions[20,21]:

$$y(x) = \pm\left(y_{edge} - y_{facet}\right)\exp\left(-\frac{|x|}{0.217W_{facet}}\right) + y_{facet} \quad \left(\pm : \text{`}+\text{'} \text{ for } V_{FB}, k_e; \text{`}-\text{'} \text{ for } \eta_{sep}, k_h\right) \tag{1}$$

Here *y* denotes any of the four photoelectrochemical parameters. y_{edge} is *y*'s value at the inter-facet edge (that is, $x=0$); y_{facet} is the value intrinsic to the particle's {010} or {110} facet unaffected by inter-facet junction. W_{facet} is the width of the near-edge surface transition zone on either facet, defined as the distance from the edge where $|y - y_{facet}|$ reaches approximately 1% of $|y_{edge} - y_{facet}|$ (refs. [20,21]).

Pooling results from 73 particles of various facet sizes, V_{FB} at the edge or intrinsic to the two facets (that is, $V_{FB,edge}$, $V_{FB,\{010\}}$ and $V_{FB,\{110\}}$) shows clear facet-size dependences (Fig. 2a): smaller facets (that is, smaller $L_{\{010\}}$ or $L_{\{110\}}$) exhibit more negative V_{FB}, consistent with higher surface energies of smaller particles. $\eta_{sep,edge}$, $\eta_{sep,\{010\}}$ and $\eta_{sep,\{110\}}$ show opposite facet-size dependences to V_{FB} (Fig. 2b), as steeper SEI band bending renders more efficient charge separation in the SEI depletion zone. $W_{\{010\}}$ and $W_{\{110\}}$, the widths of the near-edge surface transition zones on the two respective facets, show no facet-size dependence (Fig. 2c), possibly because they only depend on the surface chemical compositions of respective facets, analogous to the observation that the depletion zone widths of lateral 2D junctions are solely determined by the chemical compositions (for example, dopant densities) of their constituent 2D materials[20,21]. The values of $W_{\{010\}}$ and $W_{\{110\}}$ are approximately 2,000 to 3,000 nm, quantifying the broadness of these near-edge surface transition zones and suggesting the 2D-like nature of on-particle inter-facet junctions. Furthermore, the values of near-edge surface transition zones stay consistent regardless of which photoelectrochemical property is analysed (that is, V_{FB}, η_{sep}, k_h or k_e; Fig. 2c),

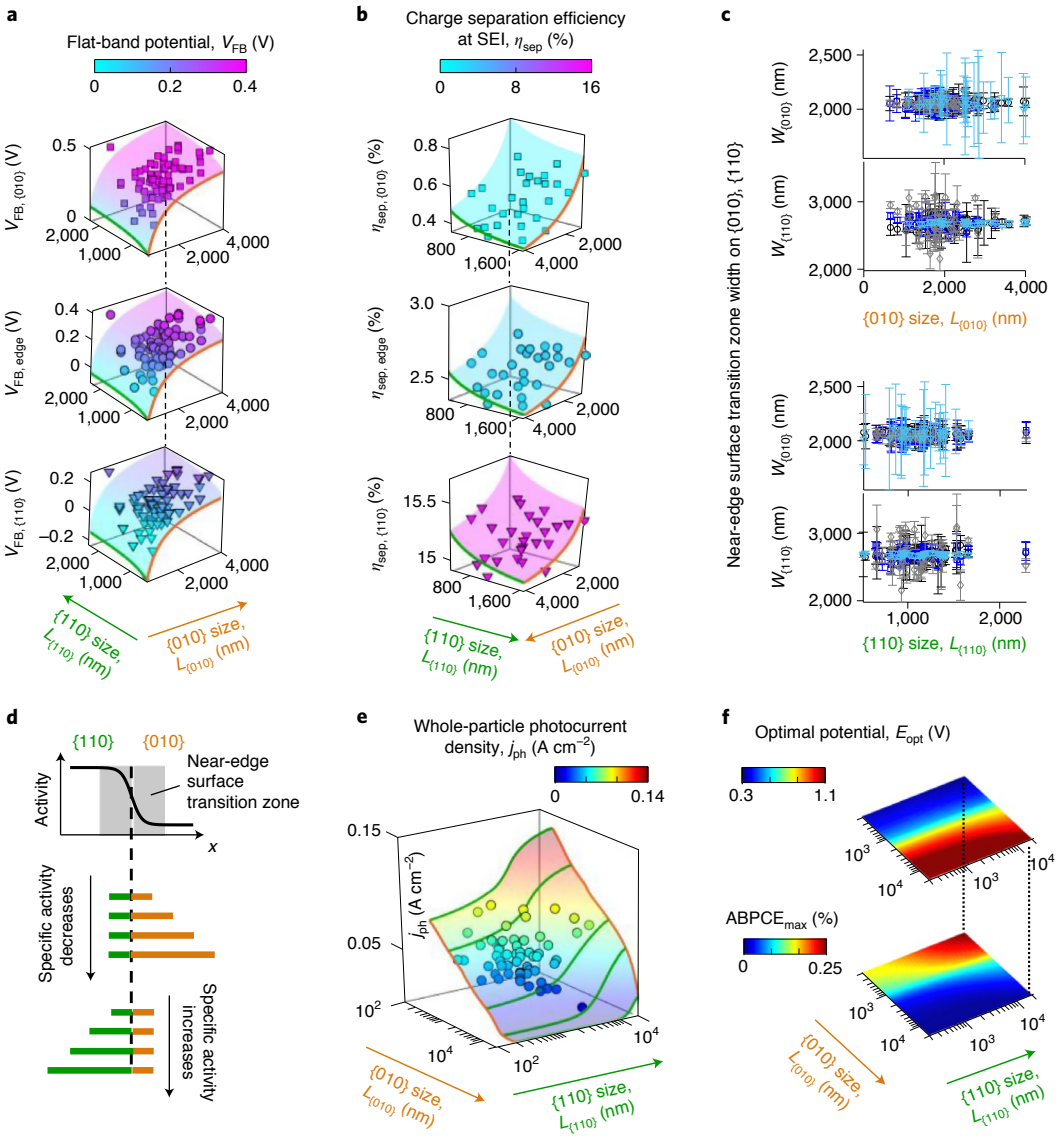

Fig. 2 | Inter-facet junctions govern whole-particle photoelectrochemistry. a,**b**, Facet-size scaling relations of intrinsic values of V_{FB} (**a**) and η_{sep} (**b**) at {010} and {110} facets, and at the interface edge. Each point represents one particle; 73 particles in **a**; 28 particles in **b**. Shaded surfaces represent fits with facet-size scaling models (Supplementary Note 2.6). **c**, Dependences of near-edge surface transition zone widths ($W_{\{010\}}$, $W_{\{110\}}$) on $L_{\{010\}}$ (top) and $L_{\{110\}}$ (bottom), derived from sigmoidal-like spatial profiles of V_{FB} (black), η_{sep} (light blue), k_h (dark blue) and k_e (grey) along the surface across the edge. Each point represents one particle. Error bar, s.d. **d**, Illustrating inter-facet junction effects on whole-particle specific photoelectrochemical activity. The orange (green) bar indicates the {010} ({110}) component. **e**, ($L_{\{010\}}$, $L_{\{110\}}$) dependences of whole-particle photoelectrochemical current densities (j_{ph}) at 1.13 V. Each circle represents the experimental result from one particle. The shaded surface represents the predictions. Orange (green) lines, j_{ph} versus $L_{\{010\}}$ ($L_{\{110\}}$) at fixed $L_{\{110\}}$ ($L_{\{010\}}$). For data at other potentials see Supplementary Fig. 16. **f**, ($L_{\{010\}}$, $L_{\{110\}}$) dependences of ABPCE$_{max}$ (bottom) and E_{opt} (top).

verifying that super-resolution charge-carrier reaction imaging indeed complements the diffraction-limited photoelectrochemical current measurements in mapping local properties associated with inter-facet junction effects.

The *s*-like spatial variations of V_{FB} and η_{sep} across the inter-facet junction along the particle surface immediately predict that for better photoelectrochemical water oxidation performance, $BiVO_4$ particles should have smaller {010} facets, minimizing the region outside the near-edge surface transition zone on the {010} facet (Fig. 2d, middle), and larger {110} facets, utilizing the entire surface transition zone and beyond on the {110} facet (Fig. 2d, bottom). Provided the facet-size dependences of $V_{FB,edge/facet}$, $\eta_{sep,edge/facet}$ and W_{facet} (Fig. 2a-c; Supplementary Note 2.6), we calculated photoelectrochemical current densities (j_{ph}) for whole particles of any facet sizes at any potential (for example, at 1.13 V where the photoelectrochemical current is dominated by water oxidation; Fig. 2e, shaded surface; Supplementary Note 2.7), which is a key photoanode performance metric.

Expectedly, j_{ph} decreases with increasing {010} facet size ($L_{\{010\}}$) at any fixed {110} facet size ($L_{\{110\}}$) (Fig. 2e, orange lines). With fixed $L_{\{010\}}$, j_{ph} initially increases with increasing $L_{\{110\}}$, and then levels off when $L_{\{110\}}$ reaches tens of micrometres (Fig. 2e, green lines). This level-off arises because: (1) {110} facet size already exceeds $W_{\{110\}}$, the width of the corresponding near-edge surface transition zone, and (2) larger {110} facets have worse $V_{FB,edge/facet}$ and $\eta_{sep,edge/facet}$ from particle-size effect (Fig. 2a,b, green lines). These calculations are

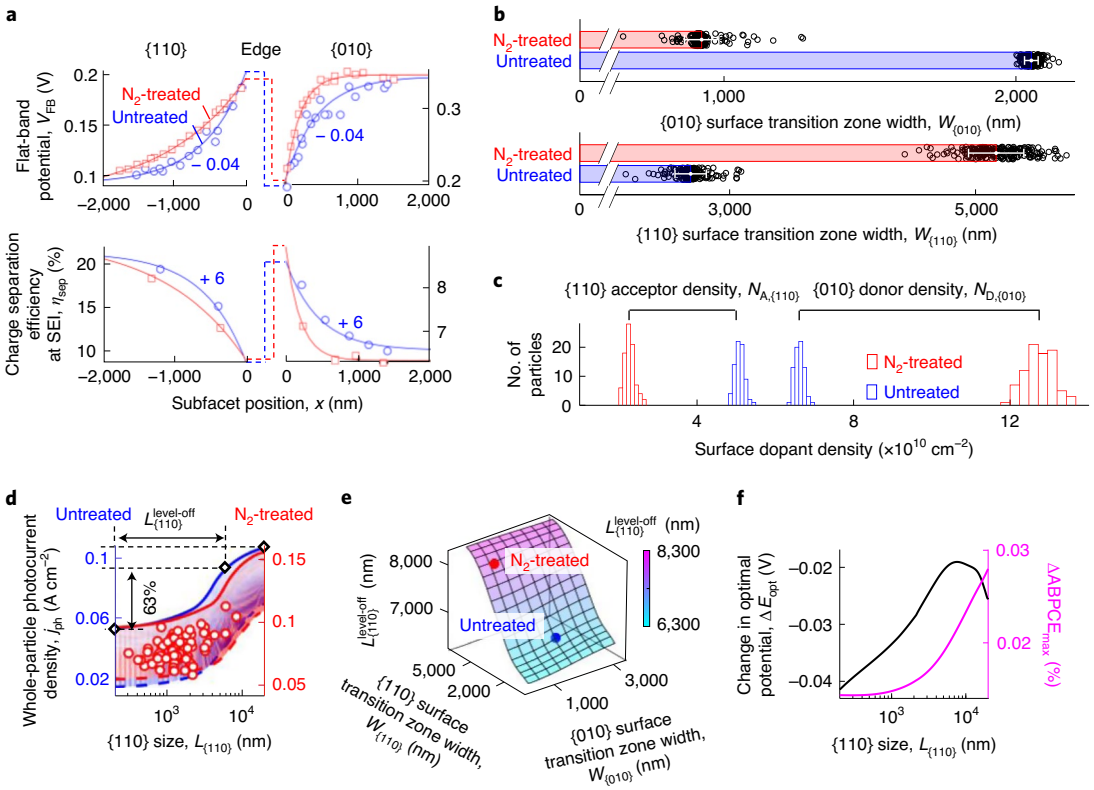

Fig. 3 | Engineering inter-facet junctions via chemical doping to modulate photoelectrode performance. a, Comparing inter-facet surface spatial profiles of V_{FB} (top) and η_{sep} (bottom) between two similarly sized, untreated ($L_{\{010\}}$ = 1557 nm, $L_{\{110\}}$ = 1520 nm) and N_2-treated ($L_{\{010\}}$ = 1566 nm, $L_{\{110\}}$ = 1751 nm) $BiVO_4$ particles. Symbols, experimental data. Solid lines, fits using equation (1). Dotted lines indicate continuity of solid lines. Blue numbers, *y*-axis shifts for clearer comparison. **b**,**c**, $W_{\{010\}}$ and $W_{\{110\}}$ (**b**; each circle represents one particle; error bar, s.d.), and $N_{D,\{010\}}$ and $N_{A,\{110\}}$ (**c**) for untreated and N_2-treated $BiVO_4$. **d**, Comparing {110}-size dependences of j_{ph} at 1.13 V between untreated and N_2-treated $BiVO_4$ at selected {010} sizes (500–5,000 nm). Each red circle represents one N_2-treated particle. The red surface represents the predictions as in Fig. 2e. The blue surface is from Fig. 2e. Double-ended arrows define $L^{level\text{-}off}_{\{110\}}$. For data at other potentials with full facet-size ranges see Supplementary Fig. 17. **e**, Simulated ($W_{\{010\}}$,$W_{\{110\}}$) dependences of $L^{level\text{-}off}_{\{110\}}$ at a representative $L_{\{010\}}$ (3,000 nm). Circles, experimentally determined from **d**. **f**, N_2-treatment -caused changes in E_{opt} (left axis) and $ABPCE_{max}$ (right axis) at a representative $L_{\{010\}}$ (3,000 nm).

verified by an experiment (Fig. 2e, circles; Supplementary Fig. 16), wherein we used an iris to confine the laser illumination to excite single whole particles to measure the whole-particle photoelectrochemical currents (Fig. 1c, right). Furthermore, given calculated photoelectrochemical current versus potential relations (Supplementary Fig. 5j,k), we determined the maximally achievable applied-bias photon-to-current efficiency ($ABPCE_{max}$), another key photoelectrode performance metric[4], and the corresponding optimal potential (E_{opt}), for particles with any facet sizes (Fig. 2f). Altogether, these facet-size scaling relations of j_{ph}, $ABPCE_{max}$, and E_{opt} (Fig. 2e,f) offer quantitative guidelines to optimize performance and operation of shaped particulate photoelectrodes by tuning junction-forming facet sizes.

Inter-facet junction engineering by chemical doping

The functional roles of the inter-facet junction raise the possibility of engineering it to alter whole-particle photoelectrochemistry. According to theory[21], the widths of surface depletion zones depend on the surface dopant densities (equations (S31)–(S33)). We therefore thermally treated $BiVO_4$ particles in nitrogen (N_2) to introduce nitrogen (confirmed by X-ray photoelectron spectroscopy; Supplementary Fig. 8d) and increase oxygen vacancies[31], which should change the particle's surface dopant densities. The N_2-treated particles maintain truncated bipyramid morphologies (Supplementary Fig. 8b); they also exhibit (sub)facet-dependent electron/hole activities (Supplementary Note 2.11) and *s*-like spatial variations of V_{FB} and η_{sep} along the surface across the inter-facet edge, characteristic of the inter-facet junction effects (Fig. 3a, red; Supplementary Fig. 7a,b). However, compared with untreated particles, the N_2-treated particles show steeper (shallower) variations on donor-richer {010} (acceptor-richer {110}) facets away from the inter-facet edge, indicating narrower (broader) near-edge surface transition zones (Fig. 3a). Averaged over 73 untreated and 86 N_2-treated particles, the surface transition zone width on the {010} facet (that is, $W_{\{010\}}$) decreases from approximately 2,050 nm to approximately 920 nm while the surface transition zone width on the {110} facet (that is, $W_{\{110\}}$) increases from approximately 2,700 nm to approximately 5,200 nm on N_2 treatment (Fig. 3b).

Furthermore, the quantitative mapping of V_{FB} across inter-facet junctions on each particle yields facet-specific surface dopant densities (equations (S31)–(S33) in the Supplementary Information). On average, N_2 treatment increases the {010} donor density ($N_{D,\{010\}}$) by approximately 6.2×10^{10} cm^{-2} due to increased oxygen vacancies (donors)[31]; such treatment decreases the {110} acceptor density ($N_{D,\{110\}}$) by approximately 2.8×10^{10} cm^{-2} unexpectedly, which we attribute to possible partial reduction of acceptor sites (V^{5+}, Bi^{3+}) by added oxygen vacancies (Fig. 3c). Strikingly, the increase in $N_{D,\{010\}}$ is about twice the decrease in $N_{D,\{110\}}$, suggesting that oxygen vacancies are more easily generated on {010} than on {110} facets. We attribute this to the fact that the {010} facet is oxygen terminated and its near-surface region has a higher oxygen density and longer Bi–O bonds (Supplementary Fig. 9); all of these should render the

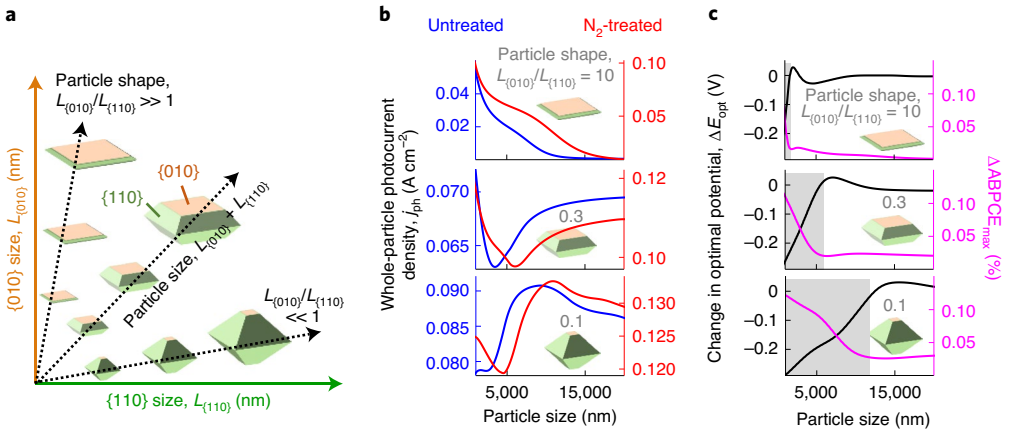

Fig. 4 | Translating inter-facet junction effects into size engineering principles of shaped particles. a, Particle-size ($L_{\{010\}} + L_{\{110\}}$) engineering with fixed particle shape (that is, at a constant $L_{\{010\}}/L_{\{110\}}$ ratio). **b**,**c**, Particle-size ($L_{\{010\}} + L_{\{110\}}$) dependences of j_{ph} at 1.13 V (**b**; left, untreated; right, N_2 treated) and N_2-treatment-induced changes in E_{opt} (left) and ABPCE$_{max}$ (right) (**c**; shades, preferred size ranges).

{010} facet more prone to oxygen loss. It is worth noting that these first-of-its-kind facet-specific doping degrees of shaped particles are only accessible by subfacet-level functional imaging.

More importantly, the changed widths of the near-edge surface transition zones of the N_2-treated particles led to altered facet-size dependences of whole-particle photoelectrochemical current densities (j_{ph}). In particular, with increasing $L_{\{110\}}$, the increase of j_{ph} levels off slower (Fig. 3d, red versus blue), due to the now broader {110} surface transition zone. To describe j_{ph}'s level-off quantitatively, we chose the characteristic {110} facet size ($L_{\{110\}}^{level\text{-}off}$) where j_{ph} increases by approximately 63% (that is, 1 – 1/e) towards its maximum (Fig. 3d). By systematically calculating surface transition zone-width dependences of $L_{\{110\}}^{level\text{-}off}$ (Fig. 3e and Supplementary Note 2.10), we find that $L_{\{110\}}^{level\text{-}off}$ correlates positively with $W_{\{110\}}$, indicating that the preferred {110} facet sizes for higher performance (where level-off occurs) increase when the {110} surface transition zones broaden, consistent with the experiment (Fig. 3e, circles).

In addition, the N_2-treated particles show enhanced photoelectrochemical currents (Fig. 3d, red versus blue; Supplementary Fig. 7e), stemming from their generally more negative flat-band potentials and higher SEI charge separation efficiencies (Supplementary Fig. 7a-b), consistent with the literature[31]. The N_2 treatment also yields more negative E_{opt} and higher ABPCE$_{max}$ (Fig. 3f), indicating better performance. Altogether, these results demonstrate that engineering inter-facet surface junctions on anisotropically shaped semiconductor particles effectively modulates their photoelectrochemical performance.

Size engineering principles of particulate photoelectrodes

Provided the quantified inter-facet junction effects and decoupled facet-size ($L_{\{010\}}$, $L_{\{110\}}$) dependences of key photoelectrode properties (for example, Fig. 2e,f), we can predict the effects of overall particle size (that is, $L_{\{010\}}+L_{\{110\}}$) for any particularly shaped particle (measured by $L_{\{010\}}/L_{\{110\}}$ for plate, truncated bipyramid or bipyramid-like shapes) on photoelectrode performance (Fig. 4a). Such quantitative prediction is needed because both the size and shape (that is, facet composition) of a particle affect its overall photoelectrochemical properties. If facet composition were the only factor, one would qualitatively predict that a larger hole-accumulating {110} facet is always preferred to enhance water oxidation performance. However, larger particles (that is, larger facet sizes) in general exhibit worse water oxidation performance because of their more positive flat-band potentials (Fig. 2a) and smaller SEI charge separation efficiencies (Fig. 2b). A substantial increase in the {110} facet size will lead to worse performance. Moreover, the near-edge surface transition zone width of the inter-facet junction effects also plays an important role in the {110} facet-size dependence of whole-particle photoelectrochemistry (Fig. 3d,e). Altogether, the interplay between the particle-size effect and the facet composition effect of inter-facet junctions makes qualitative predictions impractical, and calls on quantitative predictions based on experimentally measured photoelectrochemical parameters (Fig. 4b,c).

For {010}-dominated plate-like particles (for example, $L_{\{010\}}/L_{\{110\}}=10$; Fig. 4b, top), the whole-particle photoelectrochemical current densities j_{ph} decrease monotonically with overall particle size (that is, $L_{\{010\}}+L_{\{110\}}$). Here, the particle-size effect dominates so a larger particle has lower photocurrents. For truncated bipyramid-like particles with a higher {110} fraction (for example, $L_{\{010\}}/L_{\{110\}}=0.3$; Fig. 4b, middle), with increasing particle size, the photocurrent density shows a biphasic behaviour: initially decreasing because of the particle-size effect, and then increasing when the facet composition effect kicks in (that is, a larger particle contains more higher activity region on the {110} facet outside the near-edge surface transition zone; Fig. 2d). Here the photocurrent minimum occurs at a particle size of approximately 3.5 µm, consistent with the length scales of the surface transition zones (that is, $W_{\{010\}}+W_{\{110\}}$; Fig. 3b), and it shifts to approximately 5.9 µm for N_2-treated particles due to their altered near-edge surface transition zone widths. For {110}-dominated bipyramid-like particles (for example, $L_{\{010\}}/L_{\{110\}}=0.1$; Fig. 4b, bottom), with increasing particle size, the initial decrease and subsequent increase of photocurrent density are due to similar reasons as the case of the truncated bipyramid-like particle with $L_{\{010\}}/L_{\{110\}}=0.3$, and the eventual decrease occurs because the particle-size effect dominates again. This triphasic behaviour leads to an optimal particle size for maximal j_{ph} at approximately 8.3 µm, which shifts to approximately 10.9 µm in N_2-treated $BiVO_4$ particles. Moreover, smaller particles generally show more doping-induced improvements in E_{opt} and ABPCE$_{max}$ (that is, more negative ΔE_{opt}, larger ΔABPCE$_{max}$) (Fig. 4c); the upper limit of preferred size range increases for more bipyramid-like particles (Fig. 4c, bottom versus top).

It is worth noting that such diverse shape-coupled size dependences can be uncovered only after we have quantified both the inter-facet and the intra-facet differences of local photoelectrode functional properties on single particles of various sizes, including the inter-facet junction effects. Altogether, these predictions offer quantitative photoelectrode design principles by particle-size engineering of selected morphologies, a widely adopted optimization

approach, which can often be achieved by tuning synthesis conditions[1,32–34].

Concluding remarks

With continued discoveries of anisotropically shaped semiconductor particles[1] and doping strategies[16], we envision that inter-facet junction effects can be broadly exploited. They may be further tuned by interfacing particles with cocatalysts[5,6,10] or microorganisms[35], and utilized for other technologically important (photo) electrocatalytic processes (for example, carbon dioxide reduction, N_2 fixation)[4,7,9]. In particular, the incorporation of cocatalysts will probably affect the inter-facet junction effects (Supplementary Note 2.14): the local photoelectrochemical properties of shaped particles can be altered by cocatalysts and should further depend on cocatalysts' locations relative to the inter-facet edge and associated surface transition zones on each facet. The ill-defined nature of many cocatalysts (for example, being porous and/or spatially non-uniform[36,37]) makes studying them even more challenging. Combined with spatially controlled photodeposition of cocatalysts[10], we expect that our multimodal functional imaging approach here should help elucidate such semiconductor–cocatalyst interfaces. Furthermore, with scalable and composition-tunable solution synthesis, inter-facet junction-bearing particles could potentially broaden mixed dimensional material hetero-integration strategies[16,38], expand 2D junction compositional space (for example, complex oxides)[39], and enable device configurations with unprecedented coupling effects and drastically changed properties[15,16,18,38].

Online content

Any methods, additional references, Nature Research reporting summaries, source data, extended data, supplementary information, acknowledgements, peer review information; details of author contributions and competing interests; and statements of data and code availability are available at https://doi.org/10.1038/s41563-021-01161-6.

Received: 3 April 2021; Accepted: 21 October 2021;
Published online: 24 December 2021

References

1. Chen, S., Takata, T. & Domen, K. Particulate photocatalysts for overall water splitting. *Nat. Rev. Mater.* **2**, 17050 (2017).
2. Takata, T. et al. Photocatalytic water splitting with a quantum efficiency of almost unity. *Nature* **581**, 411–414 (2020).
3. Wang, Q. et al. Oxysulfide photocatalyst for visible-light-driven overall water splitting. *Nat. Mater.* **18**, 827–832 (2019).
4. Sivula, K. & van de Krol, R. Semiconducting materials for photoelectrochemical energy conversion. *Nat. Rev. Mater.* **1**, 15010 (2016).
5. Kim, T. W. & Choi, K.-S. Nanoporous $BiVO_4$ photoanodes with dual-layer oxygen evolution catalysts for solar water splitting. *Science* **343**, 990–994 (2014).
6. Li, R. G. et al. Spatial separation of photogenerated electrons and holes among {010} and {110} crystal facets of $BiVO_4$. *Nat. Commun.* **4**, 1432 (2013).
7. Lewis, N. S. Research opportunities to advance solar energy utilization. *Science* **351**, aad1920 (2016).
8. Segev, G., Beeman, J. W., Greenblatt, J. B. & Sharp, I. D. Hybrid photoelectrochemical and photovoltaic cells for simultaneous production of chemical fuels and electrical power. *Nat. Mater.* **17**, 1115–1121 (2018).
9. De Luna, P. et al. What would it take for renewably powered electrosynthesis to displace petrochemical processes? *Science* **364**, eaav3506 (2019).
10. Sambur, J. B. et al. Sub-particle reaction and photocurrent mapping to optimize catalyst-modified photoanodes. *Nature* **530**, 77–80 (2016).
11. Chen, R. et al. Charge separation via asymmetric illumination in photocatalytic Cu_2O particles. *Nat. Energy* **3**, 655–663 (2018).
12. Laskowski, F. A. L. et al. Nanoscale semiconductor/catalyst interfaces in photoelectrochemistry. *Nat. Mater.* **19**, 69–76 (2020).
13. Würfel, U., Cuevas, A. & Würfel, P. Charge carrier separation in solar cells. *IEEE J. Photovolt.* **5**, 461–469 (2015).
14. Würfel, P. & Würfel, U. *Physics of Solar Cells: From Basic Principles to Advanced Concepts* 2nd updated and expanded edn (Wiley-VCH, 2009).
15. Novoselov, K. S., Mishchenko, A., Carvalho, A. & Castro Neto, A. H. 2D materials and van der Waals heterostructures. *Science* **353**, aac9439 (2016).
16. Liu, Y., Huang, Y. & Duan, X. Van der Waals integration before and beyond two-dimensional materials. *Nature* **567**, 323–333 (2019).
17. Ling, X. et al. Parallel stitching of 2D materials. *Adv. Mater.* **28**, 2322–2329 (2016).
18. Alcaraz Iranzo, D. et al. Probing the ultimate plasmon confinement limits with a van der Waals heterostructure. *Science* **360**, 291–295 (2018).
19. Li, M.-Y. et al. Epitaxial growth of a monolayer WSe_2-MoS_2 lateral p-n junction with an atomically sharp interface. *Science* **349**, 524–528 (2015).
20. Yu, H., Kutana, A. & Yakobson, B. I. Carrier delocalization in two-dimensional coplanar p–n junctions of graphene and metal dichalcogenides. *Nano Lett.* **16**, 5032–5036 (2016).
21. Nipane, A., Jayanti, S., Borah, A. & Teherani, J. T. Electrostatics of lateral p-n junctions in atomically thin materials. *J. Appl. Phys.* **122**, 194501 (2017).
22. Zheng, C. et al. Direct observation of 2D electrostatics and ohmic contacts in template-grown graphene/WS_2 heterostructures. *ACS Nano* **11**, 2785–2793 (2017).
23. Mariano, R. G. et al. Microstructural origin of locally enhanced CO_2 electroreduction activity on gold. *Nat. Mater.* **20**, 1000–1006 (2021).
24. Velmurugan, J., Zhan, D. & Mirkin, M. V. Electrochemistry through glass. *Nat. Chem.* **2**, 498–502 (2010).
25. Roeffaers, M. B. J. et al. Spatially resolved observation of crystal-face-dependent catalysis by single turnover counting. *Nature* **439**, 572–575 (2006).
26. Tachikawa, T., Yonezawa, T. & Majima, T. Super-resolution mapping of reactive sites on titania-based nanoparticles with water-soluble fluorogenic probes. *ACS Nano* **7**, 263–275 (2013).
27. Zhang, Y. et al. Unique size-dependent nanocatalysis revealed at the single atomically precise gold cluster level. *Proc. Natl Acad. Sci. USA* **115**, 10588–10593 (2018).
28. Ristanovic, Z., Kubarev, A. V., Hofkens, J., Roeffaers, M. B. J. & Weckhuysen, B. M. Single molecule nanospectroscopy visualizes proton-transfer processes within a zeolite crystal. *J. Am. Chem. Soc.* **138**, 13586–13596 (2016).
29. Zhou, X. C. et al. Quantitative super-resolution imaging uncovers reactivity patterns on single nanocatalysts. *Nat. Nanotechnol.* **7**, 237–241 (2012).
30. Cendula, P. et al. Calculation of the energy band diagram of a photoelectrochemical water splitting cell. *J. Phys. Chem. C.* **118**, 29599–29607 (2014).
31. Kim, T. W., Ping, Y., Galli, G. A. & Choi, K.-S. Simultaneous enhancements in photon absorption and charge transport of bismuth vanadate photoanodes for solar water splitting. *Nat. Commun.* **6**, 8769 (2015).
32. Zhao, M. & Xia, Y. Crystal-phase and surface-structure engineering of ruthenium nanocrystals. *Nat. Rev. Mater.* **5**, 440–459 (2020).
33. Honkala, K. et al. Ammonia synthesis from first-principles calculations. *Science* **307**, 555–558 (2005).
34. Somorjai, G. A. & Park, J. Y. Molecular factors of catalytic selectivity. *Angew. Chem. Int. Ed.* **47**, 9212–9228 (2008).
35. Sakimoto, K. K., Wong, A. B. & Yang, P. Self-photosensitization of nonphotosynthetic bacteria for solar-to-chemical production. *Science* **351**, 74–77 (2016).
36. Nellist, M. R., Laskowski, F. A. L., Lin, F., Mills, T. J. & Boettcher, S. W. Semiconductor–electrocatalyst interfaces: theory, experiment, and applications in photoelectrochemical water splitting. *Acc. Chem. Res.* **49**, 733–740 (2016).
37. Walter, M. G. et al. Solar water splitting cells. *Chem. Rev.* **110**, 6446–6473 (2010).
38. Bae, S.-H. et al. Integration of bulk materials with two-dimensional materials for physical coupling and applications. *Nat. Mater.* **18**, 550–560 (2019).
39. Kum, H. S. et al. Heterogeneous integration of single-crystalline complex-oxide membranes. *Nature* **578**, 75–81 (2020).

Methods

Preparation and characterization of $BiVO_4$ and nitrogen-treated $BiVO_4$. $BiVO_4$ particles with exposed {010} and {110} facets were synthesized hydrothermally using a procedure modified from that of Li et al.[6] Typically, 3 mmol ammonium metavanadate (NH_4VO_3, Sigma-Aldrich, 398128-50G) and 3 mmol bismuth(III) nitrate pentahydrate ($Bi(NO_3)_3{\cdot}5H_2O$, Sigma-Aldrich, 383074-100G) were dissolved in 30 ml of 1 M nitric acid solution (Sigma-Aldrich, 438073-500 ML), and the pH of the resulting solution was adjusted to about 1 with ammonia solution (EMD Millipore, 1054232500). Next, the solution was hydrothermally treated in a sealed 100 ml borosilicate glass bottle (Fisherbrand) inside a furnace (Thermo Scientific Lindberg/Blue M) at 80 °C for 48 h, and the yellow solid powder was then separated by filtration, followed by washing with water several times and drying in air at 60 °C for 24 h. Nitrogen-treated $BiVO_4$ was obtained by a mild thermal annealing of as-synthesized $BiVO_4$ particles in a N_2 atmosphere, based on a method modified from the literature[31]. Typically, hydrothermally synthesized $BiVO_4$ particles, after washing with water and drying in air at 60 °C, were annealed under N_2 flow inside a box furnace (Thermo Scientific Lindberg/Blue M) at 450 °C for 8 h. The furnace was equipped with a gas vent of 1′ in diameter at the top and a gas inlet of 0.375′ in diameter at the back for N_2 atmosphere exchange. The inside chamber of the box furnace was $39.4\times27.9\times22.9\,cm^3$. This annealing condition was identified to be effective in the incorporation of nitrogen atom into $BiVO_4$ under our experimental conditions, after attempting to employ a range of annealing temperatures (350–450 °C with a ramping rate of ~5–10 °C min^{-1}) and treatment times (1 h to 8 h). This effective annealing condition is slightly different from the optimal condition reported by Kim et al.[31] (annealing at 350 °C for only 2 h) probably because they used a smaller tube furnace with less heat dissipation and their $BiVO_4$ particles are generally smaller in size (~0.5–1 μm). The amount of nitrogen atoms incorporated into $BiVO_4$ here is in agreement with that obtained by Kim et al.[31] Assuming charge-balanced incorporation of nitrogen, for every two N^{3-} ions incorporated, three O^{2-} ions need to be removed, which creates one oxygen vacancy. Therefore, the formula and nitrogen-doped $BiVO_4$ can be written as $BiVO_{4-1.5x}N_x$ assuming that no other types of oxygen vacancies are present. For our nitrogen-doped $BiVO_4$, the nitrogen content, x, in $BiVO_{4-1.5x}N_x$ is estimated to be 0.37 based on the X-ray photoelectron spectroscopic (XPS) results, and is similar to the previously reported[31] value of 0.34 quantified by XPS. It was also shown that a shorter N_2 treatment time generally led to a smaller amount of incorporated nitrogen, with the N content, x, varying between 0.34 and 0.1[31]. Moreover, the location of the XPS N 1*s* peak observed in our nitrogen-doped $BiVO_4$ (Supplementary Fig. 8d) agrees with that of nitrogen incorporated into the oxide lattice[40,41]. SEM imaging (LEO 1550 FESEM) shows that both as-synthesized and N_2-treated $BiVO_4$ particles display a well-defined truncated bipyramid morphology that consists of exposed {010} and {110} facets (Supplementary Fig. 8a,b). XPS analysis (Kratos Axis Ultra instrument with a monochromatic Al Kα source) confirms, on N_2 treatment, the successful incorporation of nitrogen into the $BiVO_4$ lattice with a clear N 1*s* peak showing in the XPS spectra (Supplementary Fig. 8c,d).

Bulk photoelectrochemical measurements. Bulk-level experiments were carried out using bulk $BiVO_4$ films deposited on indium-doped tin oxide (ITO)-coated glass slides (Delta Technologies, CB-50IN-0111) in three front-illumination configurations: (1) in a quartz cell ($1\times4\times4\,cm^3$, Starna Cells, 1-Q-40) illuminated by an expanded 405 nm laser beam with an illumination area of approximately $4.5\,cm^2$; (2) in a microfluidic cell (for details, see Methods) under wide field $60\times70\,\mu m^2$ illumination (Supplementary Fig. 6, mode II); and (3) in a microfluidic cell illuminated with a focused laser spot of approximately 380 nm (Supplementary Fig. 6, mode I; Supplementary Fig. 1a,b). These three configurations allow us to access a broad range of laser power densities ranging from $1\,mW\,cm^{-2}$ to $10^6\,W\,cm^{-2}$. All photoelectrochemical measurements were performed with a potentiostat (CH Instrument, CHI1200a) in a three-electrode configuration using $BiVO_4$-modifed ITO electrodes as the working electrode, a Pt wire (BASi, MW-1033) as the counter electrode and a Ag/AgCl electrode (BASi, MF-2052) as the reference electrode. The working electrode chamber was always kept under N_2 atmosphere and the electrolyte solution was N_2 purged, deaerated 0.1 M sodium sulfate Na_2SO_4, 0.1 M pH 7.4 phosphate buffer for photocurrent measurement. In the cases of measuring charge-carrier reaction rates, hole- or electron-probe molecules[10] (50 μM hole-probe amplex red or 33 μM electron-probe resazurin) were added to the electrolyte solution. All the potentials reported in this work are referenced to RHE. The measured potentials versus silver/silver chloride electrode, Ag/AgCl ($V_{Ag/AgCl}$) are converted to potentials versus RHE (V_{RHE}) by $V_{RHE} = V_{Ag/AgCl} + 0.0591 \times pH + 0.197$[42].

Multimodal photoelectrode performance metric imaging. The detailed experimental set-up of the multimodal photoelectrode performance metric imaging is schematically illustrated in Supplementary Fig. 6 (similar to Fig. 1c), which provides capabilities to perform and correlate subfacet-level photocurrent mapping (mode I), super-resolution charge-carrier reaction imaging (mode II) and single whole-particle photocurrent measurement (mode III), which report photoelectrode performance complementary to other single-particle measurements[11,27,43]. This multimodal imaging set-up is based on epifluorescence microscopy on an inverted OLYMPUS IX71 microscope, in combination with the use of a three-electrode photoelectrochemical microfluidic cell. An appropriate combination of a flip lens (Thorlabs, N-BK7 Plano-Convex Lens) mounted on an XYZ translation stage (Thorlabs, PT3-1, 1/4-20 Taps) and an iris placed at the back port of the microscope allows flexible switching between the three different illumination configurations. $BiVO_4$ particles (as-synthesized or N_2-treated) suspended in water were spin-coated onto and sparsely dispersed on an ITO electrode (Delta Technologies, CB-50IN-0111) and annealed at 450 °C for 1 h, and then assembled into the photoelectrochemical microfluidic cell (100 μm high and 5 mm wide) using double-sided tapes sandwiched between a microscope coverslip and the ITO electrode. The electrolyte solution (deaerated 0.1 M Na_2SO_4, 0.1 M pH 7.4 phosphate buffer) or the reactant solution (the same electrolyte solution with 50 nM hole-probe amplex red or 50 nM electron-probe resazurin added)[10] was continuously supplied by a syringe pump to the photoelectrochemical cell at a volumetric flow rate of 25 μl min^{-1}. The ITO electrode with dispersed individual $BiVO_4$ particles serves as the working electrode, the electrochemical potential of which was controlled by a potentiostat (CH Instrument, CHI1200a). A platinum wire (BASi, MW-4139) and a Ag/AgCl electrode (BASi, MW-2030) were used as the counter and reference electrode, respectively, and were placed in a liquid chamber approximately 3 cm downstream. No specific treatments were used to prevent surface passivation, but the stability of $BiVO_4$ particles under operating conditions during the entire measurements was verified, including photocurrent measurements and single-molecule fluorescence imaging (Supplementary Note 2.12). All measurements used a pH of 7.4 phosphate buffer as the electrolyte solution. It has been widely reported that under near-neutral conditions $BiVO_4$ photoanodes are photoelectrochemically stable without specific modifications by surface protection layers[5,6,31,44–48], while in strong acidic and basic solutions (for example, pH 0 or 14), protection layers are usually needed to improve the stability of $BiVO_4$[49]. Studies have shown that $BiVO_4$ and ITO electrodes may form ohmic contacts with proper treatments[44,50,51]. We have followed Abdi et al.[44] using annealing at 450 °C for 1 h in air to improve the electrical contact between the $BiVO_4$ particles and ITO. In general, annealing may help form ohmic contacts between semiconductors and back contacts[52–54]. Nevertheless, there is a possibility that the $BiVO_4$–ITO interface may not be an ideal ohmic contact, and the properties of the $BiVO_4$–ITO contact may vary from particle to particle. However, even so, the subparticle location dependences of photoelectrochemical properties should not be affected because the measured quantities at different subparticle locations share the same particle–ITO contact. Such contact heterogeneity could contribute to the particle-to-particle variations in photoelectrochemical properties, but these variations are averaged out by pooling results from many particles.

Mode I: subfacet-level photoelectrochemical current mapping. A continuous wave circularly polarized 405 nm laser (COHERENT, OBIS 405LX) was enlarged by a pair of beam expanders (15CF1-TP01188123, 1CF1-TP00426869) by 15 times and focused by a ×60x= water immersion objective (OLYMPUS, UPLSAPO60XW)[10] (Supplementary Fig. 6, mode I) to generate a laser spot with a diameter of approximately 380 nm (Supplementary Fig. 1a,b) and a maximum power density of approximately $8\times10^6\,W\,cm^{-2}$. The focused laser was used to excite multiple subfacet-level local spots, one at a time, within a single $BiVO_4$ particle, scanning from the {010} facet, across the inter-facet edge, and to the {110} facet. The photocurrents associated with all subfacet locations (registered as the x coordinate—the distance between the centroid of the focused laser beam and the 1D inter-facet edge; Fig. 1b,g and Supplementary Fig. 13a–c) at a series of applied potentials from 0.23 to 1.13 V with 0.1 V increments were recorded by the potentiostat (CH Instrument, CHI1200a). The 405 nm laser power density is typically $8.73\times10^4\,W\,cm^{-2}$ for the subfacet-level photocurrent measurements in this work unless stated otherwise. The relationship between the subfacet-level photocurrent and the applied potential was fitted with equations (S2)–(S13) (Supplementary Information) based on a modified Reichman model[10,30] (Supplementary Note 1.3) to obtain the local, intrinsic materials property parameters, V_{FB} and η_{sep}, that govern photoelectrode performance.

Mode II: super-resolution charge-carrier reaction imaging. The charge-carrier reaction imaging set-up is based on single-molecule localization microscopy[26,28,55–61] with two-laser epifluorescence illumination (Supplementary Fig. 6, mode II), in combination with the use of the fluorogenic hole-probe amplex red oxidation reaction or electron-probe resazurin reduction reaction[10] (Supplementary Fig. 10a,b). A 405 nm laser (COHERENT, OBIS 405LX) with a power density of $12\,W\,cm^{-2}$ excites the $BiVO_4$ particles to generate charge carriers (electrons and holes) while a 532 nm laser (COHERENT, SAPPHIRE 532-50CW CDRH) with a power density of $60\,W\,cm^{-2}$ induces the fluorescence of the product molecule resorufin from either the hole-probe or electron-probe reaction. The two lasers were combined via a 425 nm long-pass dichroic mirror (THORLAB, DMLP425), focused onto the back aperture of a ×60 water immersion objective (OLYMPUS, UPLSAPO60XW), and reflected by a 550 nm long-pass dichroic mirror (CHROMA, E550LP) to illuminate the sample in an epi-illumination geometry over an $70\times60\,\mu m^2$ area. The fluorescence was collected through the same ×60 objective, passed through the 550 nm long-pass dichroic mirror and a 580 ± 30 nm emission filter (CHROMA, HQ580/60 m), and imaged by an electron multiplying charge coupled device camera (ANDOR, DU-897E-CS0-#BV) operated at a 15 ms frame

rate, which is controlled by the ANDOR IQ3 software. Imaging experiments were performed at a series of applied potentials from 0.23 to 1.13 V with 0.1 V increments for both the hole-probe and electron-probe reactions. In a typical charge-carrier reaction imaging experiment, for each applied potential, 1,000 fluorescence images in an electrolyte solution without adding the fluorogenic reactant (that is, amplex red or resazurin) were collected first (to measure the steady photoluminescence intensities of $BiVO_4$; Supplementary Note 1.4), followed by recoding another 30,000 fluorescence images in the presence of 50 nM amplex red or resazurin. The fluorescence images obtained are analysed by a home-written MATLAB program (Supplementary Software), which is documented in detail in our previous work[10,62,63] and briefly described in Supplementary Note 1.4. Our imaging experiments map selectively surface reactions induced by photogenerated holes or electrons at approximately 40 nm spatial resolution (Supplementary Fig. 2d,e) at a series of applied potentials. The relationship between the local hole/electron-probe reaction rates obtained on the same $BiVO_4$ particle and the applied potential was fitted globally with equations (S16)–(S20) (Supplementary Note 1.7) to obtain spatially resolved, local, intrinsic materials property parameters, V_{FB}, k_h and k_e. Notably, our fluorogenic electron and hole reaction imaging experiments were also performed while applying external biases by the potentiostat, just like the photocurrent measurements. Both electron and hole reaction imaging experiments were done under photoanodic conditions across a range of applied potentials, where the photoanodic current is dominated by water oxidation kinetics. Under these conditions, the holes are the dominant surface charge carriers, oxidizing water and, if supplied, the hole-probing profluorescent molecule amplex red. The electrons are predominantly collected by the back contact (that is, the ITO electrode), but some of them still leak to the surface, and they can be detected by the electron-probing profluorescent molecule resazurin. The ability to detect surface electrons, even under photoanodic conditions, is due to the high sensitivity of redox-selective single-molecule reaction imaging, which also has super-resolution better than the diffraction-limited resolution of subparticle photoelectrochemical current measurement. The amounts of surface holes and leaked surface electrons both depend on the applied potential (and on the facet type as well), with the former being dominant on the semiconductor surface under photoanodic conditions.

Mode III: single whole-particle photocurrent measurement. To illuminate a single whole $BiVO_4$ particle (that is, fully covering its composing {010} and {110} facets simultaneously), an expanded, collimated 405 nm laser beam was directed through an iris placed at the back port of the microscope before it was focused to the back aperture of the objective (Supplementary Fig. 6, mode III, and Supplementary Fig. 4). Hence the iris was used to adjust the illumination area so that it contains only a single whole $BiVO_4$ particle, enabling the measurement of the photocurrent coming from this specific particle. The single-whole-particle photocurrent measurements were performed at four different applied potentials (0.83, 0.93, 1.03 and 1.13 V) (Supplementary Figs. 16 and 17).

Data availability

All data needed to evaluate the conclusions in the paper are present in the paper and/or the Supplementary Information.

Code availability

MATLAB codes for data analysis and simulations supporting the findings of this study are provided with this paper.

References

40. Yang, X. et al. Nitrogen-doped ZnO nanowire arrays for photoelectrochemical water splitting. *Nano Lett.* **9**, 2331–2336 (2009).
41. Wang, J. et al. Origin of photocatalytic activity of nitrogen-doped TiO_2 nanobelts. *J. Am. Chem. Soc.* **131**, 12290–12297 (2009).
42. Ma, Y., Pendlebury, S. R., Reynal, A., Le Formal, F. & Durrant, J. R. Dynamics of photogenerated holes in undoped $BiVO_4$ photoanodes for solar water oxidation. *Chem. Sci.* **5**, 2964–2973 (2014).
43. Levin, S. et al. A nanofluidic device for parallel single nanoparticle catalysis in solution. *Nat. Commun.* **10**, 4426 (2019).
44. Abdi, F. F. et al. Efficient solar water splitting by enhanced charge separation in a bismuth vanadate-silicon tandem photoelectrode. *Nat. Commun.* **4**, 2195 (2013).
45. Ding, C. et al. Solar-to-hydrogen efficiency exceeding 2.5% achieved for overall water splitting with an all earth-abundant dual-photoelectrode. *PCCP* **16**, 15608–15614 (2014).
46. Chen, Y.-S., Manser, J. S. & Kamat, P. V. All solution-processed lead halide perovskite-$BiVO_4$ tandem assembly for photolytic solar fuels production. *J. Am. Chem. Soc.* **137**, 974–981 (2015).
47. Bornoz, P. et al. A bismuth vanadate–cuprous oxide tandem cell for overall solar water splitting. *J. Phys. Chem. C.* **118**, 16959–16966 (2014).
48. Park, Y., McDonald, K. J. & Choi, K.-S. Progress in bismuth vanadate photoanodes for use in solar water oxidation. *Chem. Soc. Rev.* **42**, 2321–2337 (2013).
49. Kim, T. W. & Choi, K.-S. Improving stability and photoelectrochemical performance of $BiVO_4$ photoanodes in basic media by adding a $ZnFe_2O_4$ layer. *J. Phys. Chem. Lett.* **7**, 447–451 (2016).
50. Hermans, Y. et al. Energy-band alignment of $BiVO_4$ from photoelectron spectroscopy of solid-state interfaces. *J. Phys. Chem. C.* **122**, 20861–20870 (2018).
51. Lee, D. et al. The impact of surface composition on the interfacial energetics and photoelectrochemical properties of $BiVO_4$. *Nat. Energy* **6**, 287–294 (2021).
52. Zhao, T. et al. A coating strategy to achieve effective local charge separation for photocatalytic coevolution. *Proc. Natl Acad. Sci. USA* **118**, e2023552118 (2021).
53. Wang, Z. et al. Ohmic contacts on silicon carbide: the first monolayer and its electronic effect. *Phys. Rev. B* **80**, 245303 (2009).
54. Porter, L. M. & Davis, R. F. A critical review of ohmic and rectifying contacts for silicon carbide. *Mater. Sci. Eng. B* **34**, 83–105 (1995).
55. Hodgson, G. K., Impellizzeri, S. & Scaiano, J. C. Dye synthesis in the Pechmann reaction: catalytic behaviour of samarium oxide nanoparticles studied using single molecule fluorescence microscopy. *Chem. Sci.* **7**, 1314–1321 (2016).
56. Chen, P. et al. Spatiotemporal catalytic dynamics within single nanocatalysts revealed by single-molecule microscopy. *Chem. Soc. Rev.* **43**, 1107–1117 (2014).
57. Zhang, Y. W. et al. Superresolution fluorescence mapping of single-nanoparticle catalysts reveals spatiotemporal variations in surface reactivity. *Proc. Natl Acad. Sci. USA* **112**, 8959–8964 (2015).
58. Chen, T. et al. Optical super-resolution imaging of surface reactions. *Chem. Rev.* **117**, 7510–7537 (2017).
59. Ng, J. D. et al. Single-molecule investigation of initiation dynamics of an organometallic catalyst. *J. Am. Chem. Soc.* **138**, 3876–3883 (2016).
60. Betzig, E. et al. Imaging intracellular fluorescent proteins at nanometer resolution. *Science* **313**, 1642–1645 (2006).
61. Rust, M. J., Bates, M. & Zhuang, X. W. Sub-diffraction-limit imaging by stochastic optical reconstruction microscopy (STORM). *Nat. Methods* **3**, 793–795 (2006).
62. Mao, X., Liu, C., Hesari, M., Zou, N. & Chen, P. Super-resolution imaging of non-fluorescent reactions via competition. *Nat. Chem.* **11**, 687–694 (2019).
63. Chen, T. Y. et al. Concentration- and chromosome-organization-dependent regulator unbinding from DNA for transcription regulation in living cells. *Nat. Commun.* **6**, 7445 (2015).

Acknowledgements

This research was supported by the US Department of Energy, Office of Science, Office of Basic Energy Sciences, Catalysis Science program, under award DE-SC0004911. It used Cornell Center for Materials Research shared facilities supported by NSF (grant no. DMR-1120296). We thank M. Hesari, N. Zou, G. Chen and W. Jung for discussions on experiment and data analysis.

Author contributions

X.M. and P.C. designed research. X.M. synthesized materials, constructed instrument, performed measurements, coded software and analysed data. X.M. and P.C. discussed results and wrote the manuscript.

Competing interests

X.M. and P.C. has filed a provisional patent (US Provisional Application no. 63/136,703) based on this work. This patent, entitled 'Materials and methods enabling two-dimensional junctions on three-dimensional particles', was filed with the US Patent and Trademark Office on 13 January 2021.

Additional information

Supplementary information The online version contains supplementary material available at https://doi.org/10.1038/s41563-021-01161-6.

Correspondence and requests for materials should be addressed to Peng Chen.

Peer review information *Nature Materials* thanks Shannon Boettcher, Patrick Unwin and the other, anonymous, reviewer(s) for their contribution to the peer review of this work.

Reprints and permissions information is available at www.nature.com/reprints.